

# Effect of Cooling Practice on the Mechanical Properties of Medium-Manganese Aluminum-Alloyed Steels after Intercritical Annealing Quench and Partition Treatment

Shahroz Ahmed,\* Olli Oja, Antti Kajjalainen, and Pasi Peura

This study reports the effect of different cooling practices after hot rolling on the microstructure and mechanical properties of intercritically annealed quench and partitioned low-carbon medium-manganese aluminum-alloyed steel. The outcomes show that the tensile strength and uniform elongation of medium-manganese steels can be improved by manipulating the cooling cycle after hot rolling. The starting microstructure, obtained after hot rolling and cooling, influences the fraction of austenite formed at the end of intercritical annealing, thereby impacting the fraction of martensite produced at the interrupted quenching step. The results illustrate that during intercritical annealing austenite tends to nucleate at a higher temperature from a ferritic microstructure compared to a microstructure consisting of mainly bainite or a mixture of ferrite, martensite, cementite, and retained austenite. Partition temperature of 400 °C facilitates the partition of carbon from martensite to austenite while partition temperature of 450 °C supports the formation of high carbon secondary martensite.

Q&P is a heat-treatment process proposed by Speer et al.<sup>[3,4]</sup> which involves complete or partial austenitization followed by interrupted quenching between  $M_s$  (martensite start) and  $M_f$  (martensite finish) temperatures, and followed by partitioning treatment for a sufficient time. Applying appropriate Q&P heat treatment to suitable steel compositions results in multiphase microstructures which leads to good balance of strength and ductility.<sup>[5–17]</sup>

Medium-manganese steels undergone Q&P treatments, with varying parameters, have been reported to show good balance of strength and elongation.<sup>[8,9,15]</sup> For example, Yan et al.<sup>[5]</sup> conducted Q&P heat treatment on a C–Mn–Si steel after intercritical annealing and full austenitization. They reported that samples subjected to intercritical annealing consisted of blocky-type retained

austenite and fine martensite laths while samples that underwent full austenitization composed of lath-type retained austenite and larger fraction of martensite. As well, they noted that intercritical annealing leads to higher fraction of retained austenite which enhances the work hardening behavior. Seo et al.<sup>[15]</sup> investigated the effect of initial quenching temperature by conducting full austenitization Q&P heat treatments on a Fe–0.21C–4.0Mn–1.6Si–1.0Cr steel. They showed that samples quenched below 210 °C offered high yield strength, samples quenched at 210 °C showed low yield strength, high tensile strength, and high work hardening rate, and samples quenched above 210 °C showed ultrahigh tensile strength but very low total elongation. Seo et al.<sup>[15]</sup> attributed this behavior to the phase fractions formed at quenching temperature. When the samples are quenched below 210 °C, high fraction of initial martensite is formed that results in high yield strength, samples quenched at 210 °C had higher fraction of retained austenite leading to high work hardening rate, and samples quenched above 210 °C contained secondary martensite resulting in low total elongation and ultrahigh strength values. Effect of partitioning time in a Q&P treatment was examined by Arlazarov et al.<sup>[8]</sup> and effect of partitioning temperature was investigated by Ayenampudi et al.<sup>[9]</sup> Arlazarov et al.<sup>[8]</sup> showed that shorter partitioning times are required to stabilize higher fraction of retained austenite when the partitioning temperature is higher than 400 °C, while Ayenampudi et al.<sup>[9]</sup> concluded that partitioning at temperatures higher than 400 °C can lead to carbide precipitation and pearlite growth. Gouné et al.<sup>[18]</sup> conducted Q&P treatment on a Fe–0.3C–2.5Mn–1.5Si wt% steel and used the partitioning temperature of


## 1. Introduction

Stringent demands for reducing the carbon emissions from automobiles have led to the development of advanced high-strength steel (AHSS) grades; novel AHSS offers high strength-to-weight ratio at the same time maintaining cost efficiency.<sup>[1]</sup> The third generation of AHSS includes carbide-free bainitic steels, medium-manganese grades, and quench and partition (Q&P) steels.<sup>[2]</sup>

S. Ahmed, P. Peura  
Engineering Materials Science  
Faculty of Engineering and Natural Sciences  
Tampere University  
Tampere 33720, Finland  
E-mail: shahroz.ahmed@tuni.fi

O. Oja  
SSAB Europe Oy, Product Development Unit  
Hämeenlinna 13300, Finland

A. Kajjalainen  
Materials and Mechanical Engineering  
University of Oulu  
Oulu 90570, Finland

 The ORCID identification number(s) for the author(s) of this article can be found under <https://doi.org/10.1002/srin.202400420>.

© 2024 The Author(s). Steel Research International published by Wiley-VCH GmbH. This is an open access article under the terms of the Creative Commons Attribution License, which permits use, distribution and reproduction in any medium, provided the original work is properly cited.

DOI: 10.1002/srin.202400420

400 °C and showed that manganese partitioning occurs at the martensite/austenite interface. They further added that there is difference in the chemical potential of manganese which extends over a distance of 5 nm at the partitioning temperature of 400 °C.

There is keen interest to investigate the nucleation and growth of austenite from disparate microstructures in various high-strength steel grades.<sup>[19–26]</sup> According to Speich et al.<sup>[19]</sup> the nucleation and growth of austenite from ferrite–pearlite microstructure occurs in three stages: 1) nucleation of austenite at pearlite–ferrite interface and rapid growth of austenite until complete dissolution of pearlite, 2) further growth of austenite from ferrite at a rate controlled by carbon diffusion in austenite, and 3) slower growth of austenite until equilibrium is reached at a rate controlled by manganese diffusion in austenite. In industrial practices, typically a soft ferrite–pearlite structure is obtained after hot rolling to control dimensional ranges in cold rolling. Although the growth of austenite from a cold-rolled full hard ferritic–pearlitic microstructure is well understood; however, there are limited studies<sup>[21,24]</sup> on the growth and nucleation of austenite during intercritical annealing from a cold-rolled microstructure consisting of bainite/martensite and or retained austenite. Specifically, the impact of distinct cold-rolled microstructures on Q&P heat-treatment parameters and the resulting mechanical properties has been scarcely reported.

In the present study, the microstructural characteristics and the mechanical properties of two different low-carbon medium-manganese aluminum-alloyed steels were investigated by conducting Q&P treatment after intercritical annealing. The starting microstructures were varied by applying different cooling practices after hot rolling to examine their effect. The aim is to report whether the strength–elongation properties of intercritically annealed low-carbon aluminum-alloyed steels can be enhanced by varying the cooling cycle after hot rolling and altering the Q&P treatment parameters.

## 2. Experimental Section

Two low-carbon medium-manganese aluminum-alloyed steels were used. The elemental compositions in wt% are shown in **Table 1**; steel 1 contains Cr and steel 2 is alloyed with Ni + Cu to increase final strength; Mo was introduced as solid solution strengthening element and to improve hardenability. Aluminum (Al) and silicon (Si) were added to inhibit carbide formation; adding Al leads to slight reduction in overall density of steels.<sup>[1,27]</sup> Furthermore, by selecting two steel compositions, we aimed to analyze the resulting phase fractions after Q&P treatments and gain a broader understanding of the findings.

### 2.1. Hot Rolling and Cooling Practice

The steels were vacuum melted and then homogenized for 2 h at 1250 °C followed by laboratory hot rolling from 55 to 3 mm with

**Table 1.** Elemental composition of investigated steels in wt%.

	C	Mn	Al	Si	Ni	Cu	Cr	Mo	S	P
Steel 1	0.26	3.2	1.7	0.8	0.04	0.01	0.46	0.44	0.004	0.008
Steel 2	0.24	3.2	1.6	0.8	0.15	0.29	0.04	0.42	0.004	0.009

the finish rolling temperature of 880 °C. Cooling to room temperature was performed using three different cooling strategies in order to obtain “three distinct” starting microstructures.

The three different hot rolling and cooling routes, named as A, B, and C, are shown in **Figure 1**. Route A is the thermomechanical route that was previously implemented in our earlier studies<sup>[28]</sup> and consists of slow cooling in furnace subsequent to hot rolling. Following hot rolling, route B samples were air cooled and intercritically annealed; steel 1 samples were intercritically annealed at 720 °C and steel 2 samples at 740 °C for 1 h. Route B was structured to refine the microstructure and obtain a contrasting starting microstructure than via route A. The intercritical annealing temperatures (IAT) were changed in route B to obtain varying fraction of prior austenite in both compositions to study the effect on the final properties. Route C consists of cooling to 600 from 880 °C, followed by slow cooling inside the furnace and intercritical annealing at 770 °C for 24 h and then slowly cooled to room temperature. Route C was designed to obtain a softer and distinct microstructure than through route A. The long intercritical annealed (IA) time in route C samples was selected to allow near-equilibrium partitioning of elements. Similar pretreatments were performed by Granbom<sup>[29]</sup> on dual-phase steels to investigate the effects of processing parameters on the microstructure and mechanical properties.

All samples were cold-rolled with ≈46% reduction to thickness of 1.6 mm. The cold-rolled sheets were cut into 110 × 15 mm samples for the intercritical annealing quenching and partitioning (IAQ&P) treatments. The long side was transversal to the rolling direction.

### 2.2. Q&P Heat Treatments

The IAQ&P treatment parameters were determined taking into account the partition of alloying elements in austenite during intercritical annealing as follows: 1) The IAT were calculated by CALPHAD software JMatPro (version 13) based on prior austenite phase fractions of 60% and 70%. Hence, the estimated IAT for steel 1 were 830 and 860 °C, while the IAT for steel 2 were 820

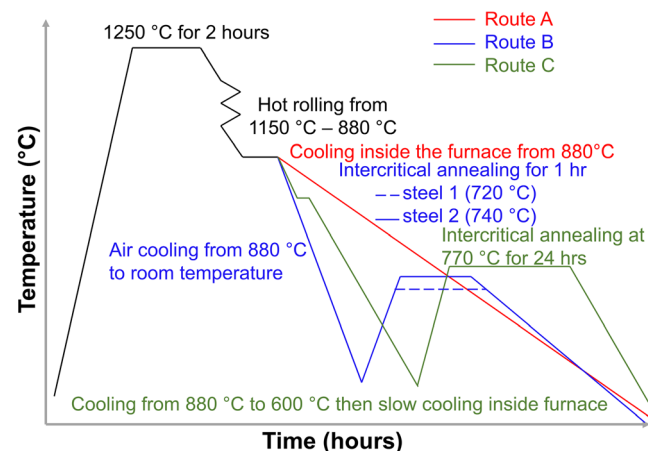


**Figure 1.** Schematic diagram showing hot rolling (black) and the cooling/processing routes A (red), B (blue), and C (green) after hot rolling.

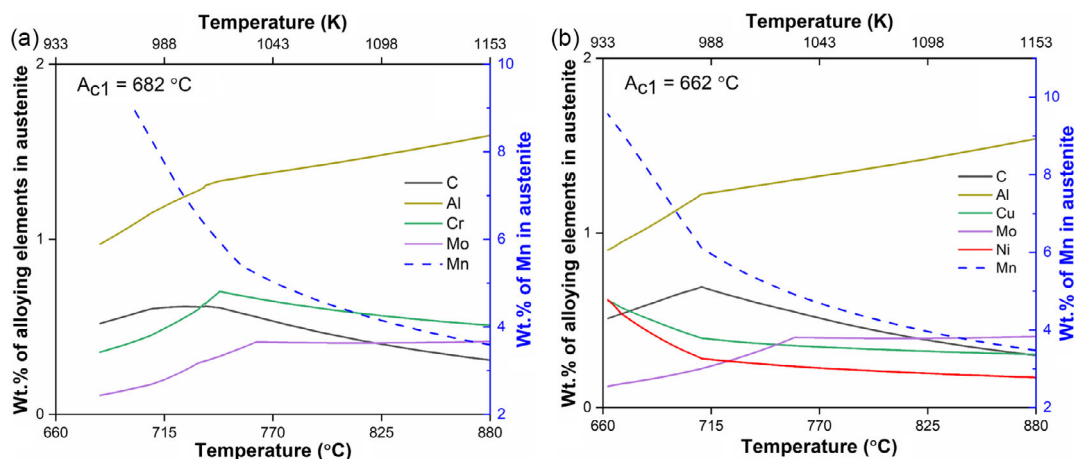


**Figure 2.** Change in the elemental composition of  $\gamma$  during heating to IAT estimated by JMatPro: a) steel 1 and b) steel 2. The scale for composition of Mn (represented by blue dashed lines) in austenite is shown on the right side of both figures. The  $A_{c1}$  calculated by JMatPro of steels are mentioned in the respective figure.

and  $850^\circ\text{C}$ . 2) The optimum quench temperature (QT), leading to maximum amount of retained austenite, was calculated using the Speer's method/model.<sup>[30]</sup> 3) The athermal progression of the austenite-to-martensite transformation was calculated using the Koistinen and Marburger equation.<sup>[31]</sup> The  $M_s$  temperature of intercritical austenite is low compared to nominal composition.<sup>[28]</sup> 4) For this reason, the composition of austenite ( $\gamma$ ) as a function of IAT was calculated using JMatPro (Figure 2) and the composition of  $\gamma$  at the fraction 60% and 70% was determined and substituted in Capdevila's  $M_s$  equation.<sup>[32]</sup> The calculated QT were  $140^\circ\text{C}$  and  $157^\circ\text{C}$  for steel 1 at 60% and 70%  $\gamma$ , respectively, while values for steel 2 were  $145^\circ\text{C}$  and  $158^\circ\text{C}$  at 60% and 70%  $\gamma$ , respectively. An example of the calculation of the amount of retained austenite plotted as a function of initial QT of steel 2 at the prior austenite fraction of 60% and 70% is presented in Figure A1, (Appendices).

The schematic diagram for the conducted IAQ&P treatments is shown in Figure 3. The steel 1 and 2 samples were initially subjected to intercritically annealed at specific IAT for 240 s then quench to calculated QT for 10 s following partitioning at  $400^\circ\text{C}$  and  $450^\circ\text{C}$  for 100 s, and quenched to room temperature. Partition temperature close to  $400^\circ\text{C}$  has been reported to be optimal in previous studies<sup>[8,9,28]</sup> but the partition temperature (PT) of

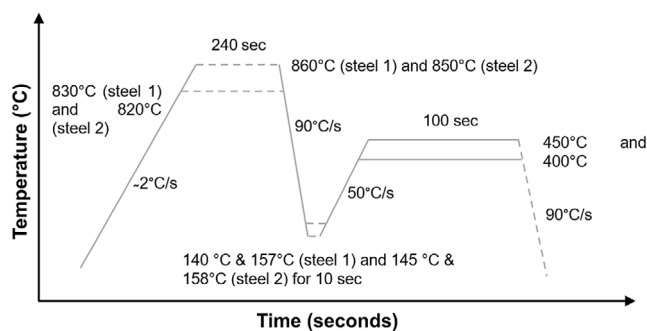


**Figure 3.** Schematic diagram of IAQ&P treatments for steels 1 and 2.

$450^\circ\text{C}$  was also used in this study to investigate the suitability of aluminum-alloyed medium-manganese steels for hot dip galvanizing and  $450^\circ\text{C}$  is close to zinc pot temperature. An austenitizing and two salt bath furnaces were used to carry out the heat treatments. One of the salt bath furnaces was used for quenching and the other one for partitioning; altogether 24 different IAQ&P heat treatments were conducted.

The IAQ&P-treated samples were cut into two pieces of  $70 \times 15 \text{ mm}$  and  $40 \times 15 \text{ mm}$ ; the longer sample was used to conduct mechanical tests and the shorter sample was used for microstructural characterization.

### 2.3. Characterization Methods

The characterization was performed in two stages; first, the initial microstructures of both steel compositions undergone cooling routes A, B, and C were studied. In the second stage, the microstructure and mechanical properties of the samples after IAQ&P treatments were investigated.

The hardness values were determined using Vickers hardness tester at a load of 200 g on the samples before IAQ&P treatments. The samples for hardness tests were prepared by usual metallographic techniques. Tensile specimens with a gauge length of 15 mm and a gauge width of 4 mm were prepared from 70 mm IAQ&P-treated samples. The tensile tests were conducted using an Instron 8800 uniaxial servohydraulic materials testing machine at a strain rate of  $2.5 \times 10^{-4} \text{ s}^{-1}$ ; the direction of loading was transverse to the direction of rolling. For strain measurements, a LaVision SMC 5M-140 optical extensometer with Davis software for digital image correlation was used. The frame rate in the image recording was 2 Hz and strain was calculated by Davis software for every frame relative to the first frame acquired.

The volume fraction of retained austenite and the carbon content in retained austenite was measured by X-ray diffraction (XRD) using Panalytical Empyrean X-ray diffractometer (Malvern Panalytical Ltd., UK), according to the ref. [33]. The XRD patterns were generated using cobalt cathode

( $40^\circ < 2\theta < 130^\circ$ ) operated at 40 kV and 45 mA and a  $0.013^\circ$  step size with 80 s per step. The analyzed peaks for austenite were (111), (200), (220), and (311). The carbon content in austenite was calculated using the Dyson and Holmes equation.<sup>[34]</sup> The samples for XRD were prepared by coarse and fine grinding with a 800 and 2000 grit SiC papers, respectively, and then electropolished using Struers LectroPol-5 with A2 as electrolyte.

The microstructural and composition analyses of the samples were conducted using Zeiss ULTRaplus field emission scanning electron microscope (SEM) equipped with energy-dispersive spectrometer (EDS) (Oxford Instruments X-MaxN 80 EDS). The SEM-EDS samples were prepared by coarse and fine grinding with SiC grit papers followed by polishing using diamond suspensions of 6, 3, 1  $\mu\text{m}$ , and the final polishing was done using colloidal silica suspension; finally, the samples were etched with 2% nital.

Crystallographic and phase analyses of the samples were conducted using Oxford Instruments Symmetry electron backscatter diffraction (EBSD) detector. The EBSD samples were cut directly from the heat-treated specimens and prepared using JEOL IB-19530 cross section polisher. The EBSD data for all samples were acquired using an accelerating voltage of 15 kV, working distance

of 12 mm, on a  $15 \times 15 \mu\text{m}^2$  area and a 25 nm step size. The obtained EBSD data were analyzed by AZtecCrystal 3.0.

Determination of phase transformation temperatures was conducted by dilatation measurements with Gleeble 3800 thermomechanical simulator.

### 3. Results

The hardness measurements, SEM, and SEM-EDS analyses of the starting microstructures of steel 1 and steel 2 after undergoing processing routes A, B, and C are presented in Section 3.1. Section 3.2 presents the results from microscopic features, mechanical behavior, and dilatation data of investigated steel compositions (undergone hot rolling and cooling routes A, B, and C) after IAQ&P treatments.

#### 3.1. Characterization of Initial Microstructures

The resulting microstructures of hot- and cold-rolled steels 1 and 2 from routes A, B, and C are shown in Figure 4 and 5.

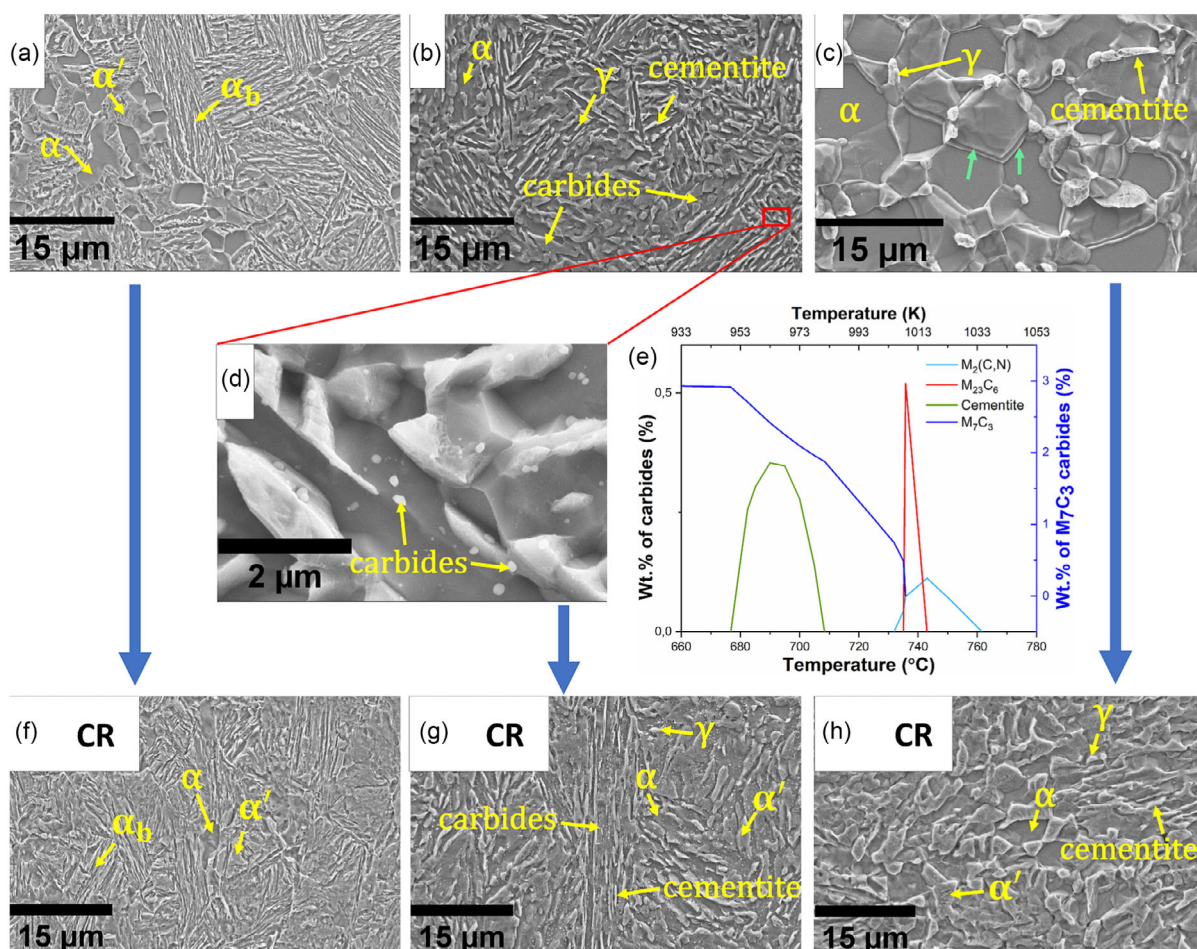


**Figure 4.** Microstructures of steel 1, hot rolled and cooled with a) route A, b) route B, and c) route C; the green arrows in the image represent regions that have been slightly overetched; d) the magnified image from a section of (b) showing carbides and e) the simulation results from JMatPro showing the type of carbides in steel 1 at the IAT between 660 and 780  $^\circ\text{C}$ ; notice the scale of  $M_7C_3$  carbides on the right. The cold-rolled (CR) microstructures after each cooling route are shown in f) route A, g) route B, and h) route C. The blue arrows represent cold rolling after each cooling route of the respective sample.

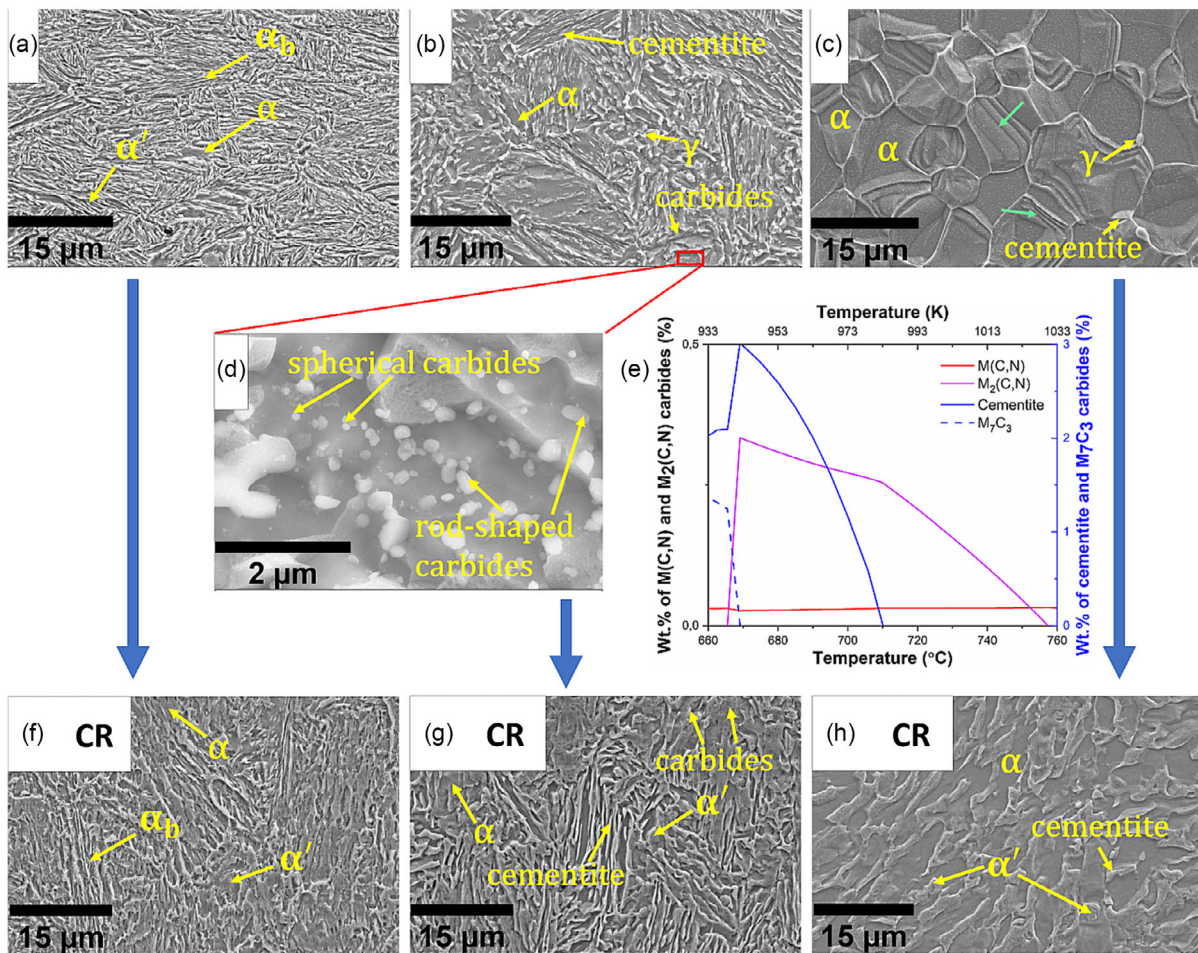


**Figure 5.** Microstructures of steel 2, hot rolled and cooled with a) route A, b) route B, and c) route C; the green arrows in the image represents the region that has been slightly overetched; d) the magnified image from a section of (b) showing small carbides and e) the simulation results from JMatPro showing the type of carbides in steel 2 at the IAT of 660–760 °C; notice the scale of cementite and  $M_7C_3$  carbides on the right. The cold-rolled (CR) microstructures after each cooling route are shown in f) route A, g) route B, and h) C. The blue arrows represent cold rolling after each cooling route for the respective sample.

The results of subsequent hardness measurements are shown in **Figure 6**. The microstructure of steel 1 after route A (Figure 4a) majorly consists of bainite ( $\alpha_b$ ), some ferrite ( $\alpha$ ), and small fraction of martensite ( $\alpha'$ ), meaning that there are also large deviations in the hardness (as shown in Figure 6) which is the cause of mixture of soft and hard phases. A magnified image of Figure 4a is presented in Figure A2. After cold rolling (Figure 4f), deformation was seen in bainite and ferrite but minor deformation was detected in martensite. The hardness also increased after cold rolling due to work hardening and there was a large deviation of  $\pm 90$  HV. Steel 1 undergone route B (Figure 4b) shows a heterogenous microstructure consisting of ferrite, cementite, 20.4% of austenite ( $\gamma$ , calculated from XRD), and carbides of size 200–300 nm, measured from high-resolution SEM micrographs (Figure 4d). JMatPro calculations (Figure 4e) show the estimate of phases and reveal that carbides might be of type  $M_7C_3$ ,  $M_{23}C_6$ , or  $M_2(C,N)$ . EDS analysis showed that these carbides either contain chromium or manganese. Further SEM investigations indicated that these carbides are located near the ferrite boundaries.

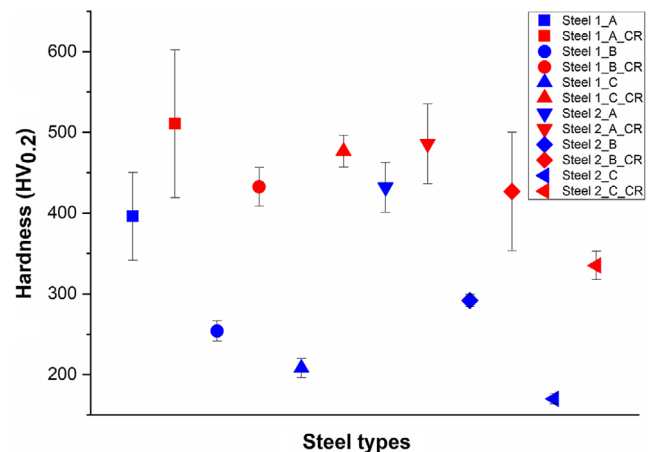


**Figure 6.** Hardness of investigated steels (average of five measurements) before IAQ&P treatments. The blue color represents steel samples before cold rolling (CR in the image legend) and red color represents hardness after cold rolling.

After cold rolling, the microstructure of route B samples (Figure 4g) consists of strained ferrite, cementite, martensite (transformed from austenite), carbides, and 3.2% of austenite. The increase in hardness after cold rolling (Figure 6) was large due to the presence of martensite and deformed ferrite. The microstructure of steel 1 from route C, presented in Figure 4c, consists of large polygonal ferrite grains,<sup>[35]</sup> cementite, and 3.2% of austenite located along the grain boundaries of ferrite; the hardness was  $208 \pm 13.4$  HV resulting mostly from high fraction of polygonal ferrite. Post-cold-rolled microstructure is shown in Figure 4h and consists majorly of strained ferrite, some martensite, cementite, and 1.4% of austenite.

The micrographs of steel 2 (Figure 5a) from route A majorly consist of bainite and small fractions of martensite and ferrite. A higher magnification image of Figure 5a is shown in Figure A2. The hardness of steel 2 from route A before cold rolling is slightly higher (Figure 6) compared to steel 1 which is due to lower ferrite fraction. The microstructure after cold rolling consists of small amount of martensite, deformed bainite, and ferrite as shown in Figure 5f. Steel 2 obtained from route B (Figure 5b) prior to cold rolling consists of cementite, ferrite, 19% of austenite, and spherical and rod-shaped carbides in size of 50–300 nm (measured from SEM micrographs). The micrograph of these carbides is shown in Figure 5d. JMatPro simulation presented in Figure 5e provides an estimation of the carbide phase fraction and demonstrates that carbides are cementite, or of type  $M_2(C,N)$  and  $M(C,N)$ . Further, SEM investigations and EDS analysis showed that these carbides are rich in manganese and are located at ferrite boundaries, similar to the carbides seen in steel 1 (Figure 4d). After cold rolling of steel 2 from route B (Figure 5g), the microstructure contains cementite, ferrite, 4.6% of austenite, martensite, and carbides. The microstructure from route C of steel 2, presented in Figure 5c, shows large fraction of polygonal ferrite, 2.1% of austenite located at ferrite grain boundaries, and small amount of cementite. After cold rolling the microstructure of steel 2 from route C consists of deformed ferrite, martensite, and cementite (Figure 5h) while any austenite was not detected.

### 3.2. IAQ&P Heat Treatments

Samples after IAQ&P are named after their steel type, obtained route, calculated austenite fraction at IAT, and PT. For example, sample “1A\_60 $\gamma$ \_450” means steel 1 obtained from route A, IA at temperature where 60% of prior  $\gamma$  was present and partitioned at 450 °C.

#### 3.2.1. XRD

The retained austenite ( $\gamma_r$ ) fraction and the carbon content in  $\gamma_r$  after IAQ&P treatments are shown in Figure 7. The fraction of  $\gamma_r$  and the carbon content in  $\gamma_r$  are generally low in route A and B samples partitioned at 450 °C compared to samples partitioned at 400 °C. Higher carbon content in  $\gamma_r$  indicates that most of the carbon is partitioning to austenite when the PT is 400 °C while less carbon is partitioning to austenite at the PT of 450 °C. Results from Figure 7 demonstrate that fraction of  $\gamma_r$  also depends on the initial microstructure because route C samples

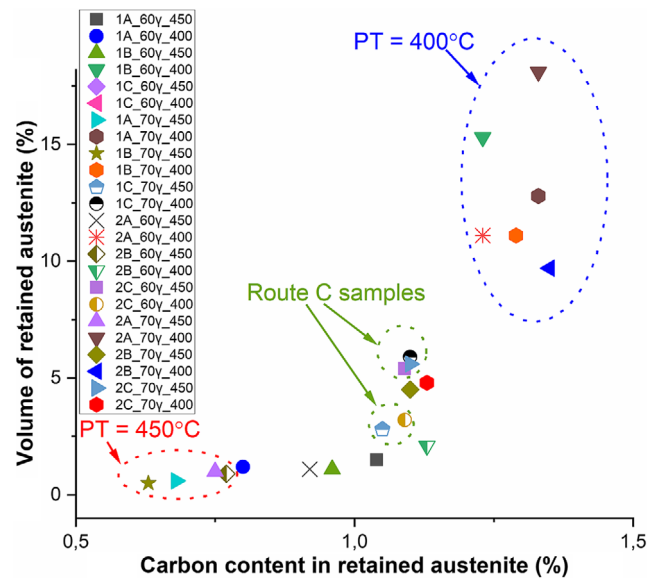


**Figure 7.** Volume fraction of retained austenite and carbon content in retained austenite measured by XRD after IAQ&P treatments.

had low amount of  $\gamma_r$ , irrespective of the PT. Further observations from Figure 7 entail that the carbon in  $\gamma_r$  is slightly higher in route C samples compared to those of route A and B samples partitioned at 450 °C. Samples 1C\_60 $\gamma$ \_450 and 1C\_60 $\gamma$ \_400 did not show any peaks of austenite in the XRD measurements, therefore they are not shown in Figure 7.

#### 3.2.2. Uniaxial Tensile Tests

Strength and uniform elongation data, presented in Figure 8a, obtained from the tensile tests demonstrate that most samples of steels 1 and 2 partitioned at 400 °C produced via the route A and B show good balance of strength and ductility, i.e., tensile strength in the range of 1350–1550 MPa and uniform elongation between 8–12.5%. These samples contain higher fraction of high carbon  $\gamma_r$  as shown in Figure 7. Route A and B samples partitioned at 450 °C show high tensile strength level but low uniform elongation, while the route C samples had the lowest tensile strength among all samples. Yield strength was determined from the stress–strain data by 0.2% offset method and are shown in Figure 8b. The yield strength of the samples from routes A and B, partitioned at 400 °C, was in the range of 700–850 MPa while samples partitioned at 450 °C had high yield strength (shown by red oval in Figure 8b) and the yield strength of route C samples was in the range of 500–600 MPa. High tensile strength and yield strength values in route A and B samples indicate higher fraction of martensite ( $\alpha'$ ); samples partitioned at 450 °C might contain more  $\alpha'$  than those partitioned at 400 °C while low strength values of route C samples indicate that they might contain lowest fraction of  $\alpha'$ .<sup>[36]</sup> The engineering stress–strain curves of selected samples are presented in Figure 8c. These curves show different mechanical behavior when the starting microstructure and IAQ&P treatment parameters are varied. Sample 1B\_60 $\gamma$ \_450 showed brittle behavior and failed immediately after

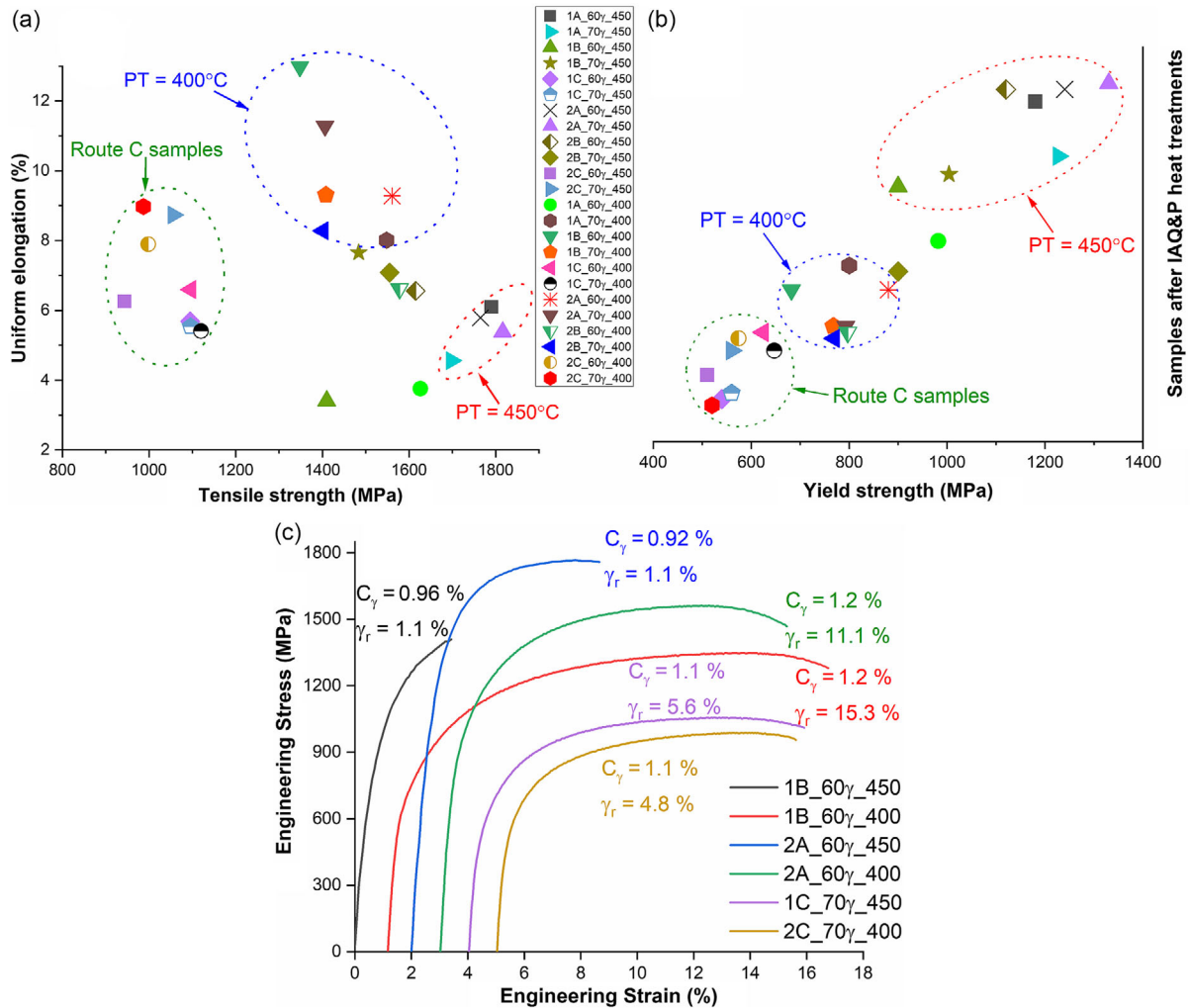


**Figure 8.** a) Uniform elongation and tensile strength after IAQ&P treatments calculated from uniaxial tensile tests b) corresponding yield strength of the samples. c) Engineering stress–strain curves of selected samples, for each curve the carbon content in  $\gamma_r$  (denoted by “ $C_\gamma$ ” only in this Figure) and  $\gamma_r$  fraction of the sample is mentioned with the respective color (note: curves starting at 0, 1%, 2%, 3%, 4%, and 5%).

yielding. Sample 2A\_60 $\gamma$ \_450 containing same amount of  $\gamma_r$  and similar carbon content in  $\gamma_r$ , had higher strength and better elongation but exhibited brittle properties. In the sample 1B\_60 $\gamma$ \_400 high amount of  $\gamma_r$  transformed to  $\alpha'$  improving the total elongation up to 16%. 2A\_60 $\gamma$ \_400 had lower fraction of  $\gamma_r$ , exhibiting lower elongation value and higher strength.

### 3.2.3. Electron Microscopy

The SEM micrographs of selected samples after IAQ&P treatment are shown in Figure 9a–i. Samples partitioned at 450 °C (Figure 9a,b,d,g) show the presence of higher fraction of secondary martensite ( $\alpha'_s$ ) and low content of primary martensite ( $\alpha'_p$ ) and  $\gamma_r$ ; the presence of  $\alpha'_s$  in the samples partitioned at 450 °C was also reported by Ayenampudi et al.<sup>[9]</sup> Secondary martensite is differentiated from primary on the basis of etching; primary

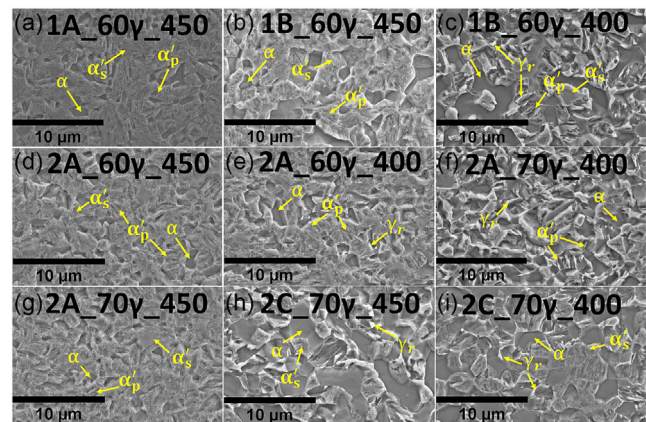


**Figure 9.** a–i) SEM micrographs of the samples after IAQ&P heat treatments.

martensite undergoes tempering during partitioning step in a Q&P treatment and is easily etched as compared to secondary martensite.<sup>[37]</sup> High fraction of  $\alpha'_s$  seems to be the reason for brittle nature of samples partitioned at 450 °C, as shown in Figure 8c. In contrast, samples partitioned at 400 °C (Figure 9c,e,f) show higher fraction of  $\alpha'_p$  and  $\gamma_r$  but low content of  $\alpha'_s$ , leading to a good balance of strength and ductility (Figure 8a,c). In the route C samples, change of PT did not affect the microstructure because both samples showed similar phases (Figure 9h,i). Samples from routes A and B (Figure 9a–g) contain higher fraction of  $\alpha'$  (either  $\alpha'_p$  or  $\alpha'_s$ ) than the route C samples which have lower fraction of  $\alpha'$  (Figure 9h,i). This means that amount of austenite is lower at the end of IAT in route C samples compared to route A and B samples, leading to lower fraction of  $\alpha'$  in the final microstructure. Comparison of the micrographs in the Figure 9 shows that there is slightly more  $\alpha$  in steel 1; probable reason is the change in chemical composition of steels which led to slightly higher  $A_{c1}$  transformation temperature of steel 1 (Figure 2).

EBSD micrographs of selected samples showing band contrast overlaid with phase maps are presented in Figure 10a–f. The effect of changing the PT can be seen by comparing the micrographs shown in Figure 10a,c and 10b,d. The samples from routes A and B subjected to PT of 450 °C show low fraction of  $\gamma_r$  while samples that were partitioned at 400 °C demonstrate comparatively higher fraction of  $\gamma_r$ . The amount of  $\alpha$  is large in route C samples (Figure 10e,f) when compared to route A and B samples that contains small amount of recrystallized  $\alpha$ .  $\alpha'$  and  $\alpha$  are distinguished on the basis of band contrast or image quality maps; a low pattern quality (dark gray regions in Figure 10) represents  $\alpha'$ . Some cementite, typically below 2%, was found in all samples at the boundaries of  $\alpha'$ . Two different morphologies of  $\gamma_r$  were seen, blocky  $\gamma_r$  ( $\gamma_{rb}$ , shown by orange arrow in Figure 10) and lath type  $\gamma_r$  ( $\gamma_{rl}$ , shown by green arrows). Sample 1B\_60 $\gamma$ \_400 consists of higher amount of  $\gamma_{rb}$  at the

boundaries of  $\alpha'$  and  $\alpha$ , while sample 2A\_60 $\gamma$ \_400 contains more  $\gamma_{rl}$  close to  $\alpha'$  laths. The higher amount of  $\gamma_{rl}$  in sample 2A\_60 $\gamma$ \_400 (Figure 10d) is probably cause of large fraction of  $\alpha'$ , while  $\gamma_{rb}$  is favored at low  $\alpha'$  fraction,<sup>[38]</sup> as shown in sample 1B\_60 $\gamma$ \_400 (Figure 10b). The presence of mechanically stable  $\gamma_{rl}$  is the reason that sample 2A\_60 $\gamma$ \_400 exhibits high work hardening rate (shown in Figure 8c).<sup>[39–41]</sup> Comparing samples of same type but with different PT, such as sample 1B\_60 $\gamma$ \_450 (Figure 10a) and sample 1B\_60 $\gamma$ \_400 (Figure 10b), it is apparent that the phases are non-homogenously distributed and the fraction of recrystallized  $\alpha$  varies. Another example of the heterogeneity is seen in the comparison of Figure 10e,f; sample 2C\_70 $\gamma$ \_450 has larger  $\alpha$  grains than 2C\_70 $\gamma$ \_400 although the heat-treatment parameters are similar. The uneven distribution of phases (especially  $\alpha$ ) indicates that there is banding in the initial microstructure.

### 3.2.4. Dilatation Measurements

For a more comprehensive understanding of the effect of initial microstructure on phase fractions, all 24 IAQ&P treatments were repeated using thermomechanical simulator with same heat-treatment parameters as shown in Figure 3. Figure 11a presents the measured  $A_{c1}$  transformation temperatures during heating to IAT, proving that  $A_{c1}$  is low in the route A and B samples compared to route C, this is particularly visible in steel 1 samples; similar observations were also reported by Esin et al.<sup>[25]</sup> Steel 2 samples obtained from routes A and B show scatter in the  $A_{c1}$  transformation temperatures which may occur due to heterogeneity of the microstructure or due to limitations of the dilatometer. Simulation results from JMatPro (Figure 2) show that  $A_{c1}$  is 682 and 662 °C for steel 1 and steel 2, respectively. Results from Figure 11a demonstrate that  $A_{c1}$  transformation temperature is not only a function of the nominal composition but also varies with the initial microstructure. Figure 11b presents the change in length of selected samples during holding at IAT. There is continuous decrease in route A and B samples and a slight increase in route C samples. The observed changes in length can originate either from the growth or nucleation of  $\gamma$  during holding at IAT; however, from the dilatation data it cannot be confirmed that whether it is growth or nucleation of  $\gamma$  but in either case the fraction of  $\gamma$  increases with the length change.<sup>[42]</sup> Figure 11b gives evidence that fraction of prior  $\gamma$  in route C samples is low as compared to route A and B samples because the change in length during holding at IAT for 100 s was minimal in route C samples; note that the change in length is positive in route C samples, this is an anomaly due to endothermic transformation of  $\alpha$  to  $\gamma$ . Figure 11c illustrates the calculated  $M_s$  temperatures and changes in dimensions of the samples (shown in Figure 11b) during cooling to QT after holding at IAT. The change in length of the samples indicated about the fraction of  $\alpha'$  formed at the quenching stage,<sup>[42]</sup> for example, higher change is seen in sample 2B\_70 $\gamma$ \_400 compared to sample 1C\_60 $\gamma$ \_400, illustrating that fraction of  $\alpha'$  is higher in the prior sample. Furthermore,  $\alpha'$  content in route C samples is low when compared to route A and B samples due to the low  $\gamma$  fraction formed at the end of IA. Due to the absence of notable deviations in the linearity of the dilatation curves, the determination of the  $M_s$  temperature

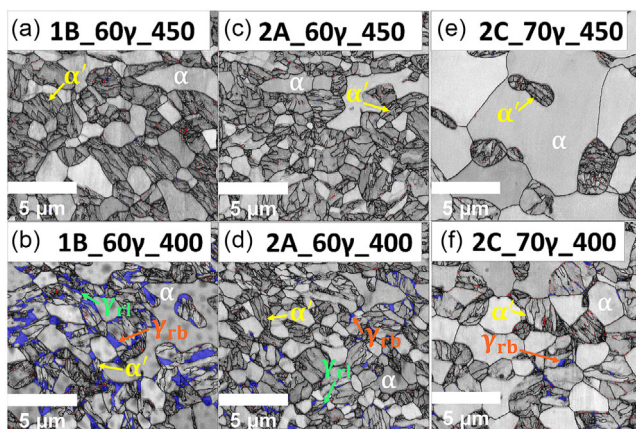


**Figure 10.** a–f) EBSD micrographs showing band contrast overlaid with grain boundaries and phase maps. The dark gray contrast represents  $\alpha'$  (also shown by yellow arrows) and light gray regions are  $\alpha$ , high-angle grain boundaries are shown by black lines, and low-angle grain boundaries are shown with white. FCC phase is shown by blue and cementite is shown by red. The light black dots seen in (b) are a cause of sample preparation.

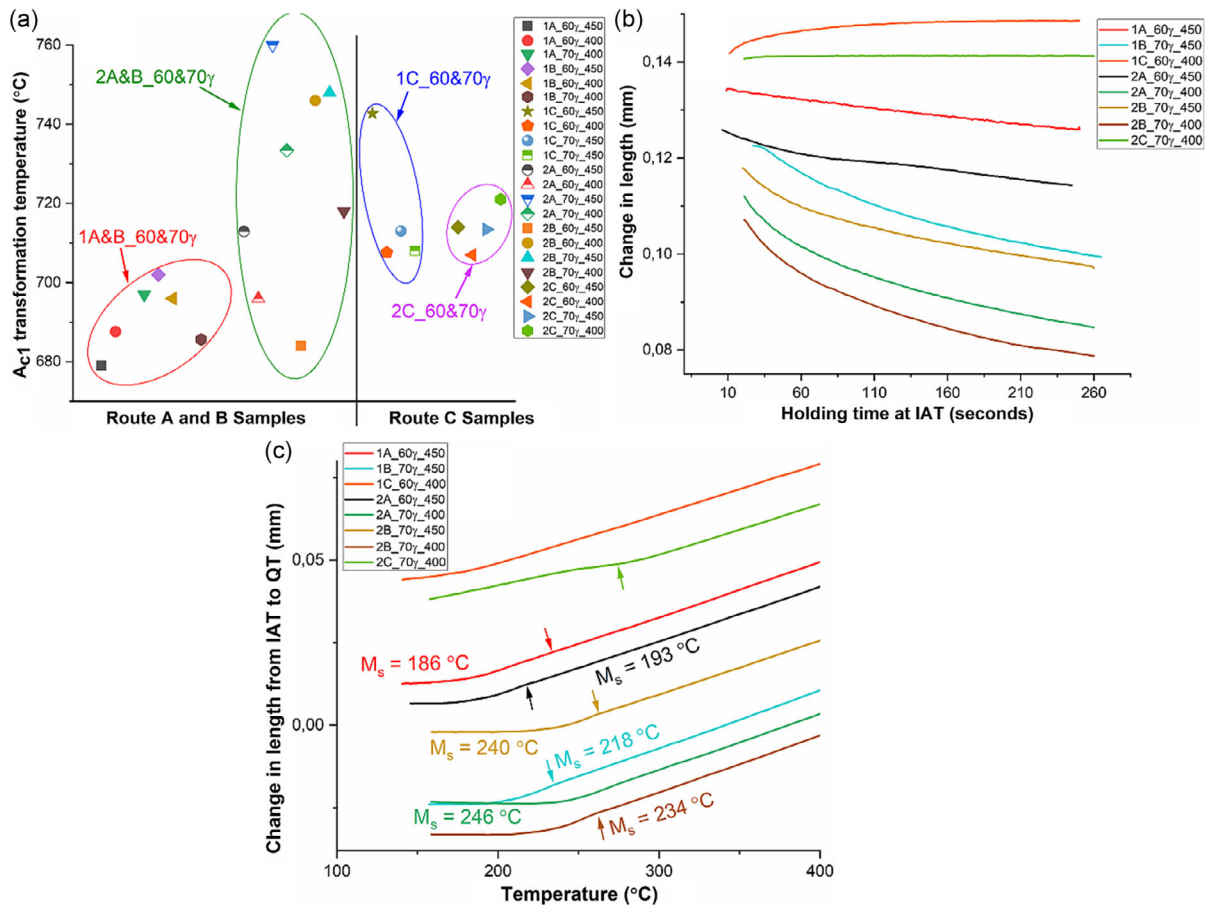


**Figure 11.** Data extracted from dilatometry experiments: a) calculated  $A_{c1}$  phase transformation temperature during heating to IAT, b) dilatometric curve during holding at IAT of selected samples, and c) dilatometric curve during cooling to QT shown with calculated  $M_s$  temperature; note that the x-axis has been reduced for clarity.

for route C samples was inconclusive. The probable reason is the high carbon content  $\gamma$  in route C samples (Figure 7), thus high stability of  $\gamma$ . From Figure 11c, it can also be seen that there is small change in linearity of the dilatation curves before  $M_s$ , pointed by small same color arrows on the respective curves. This phenomena indicates that there is small localized transformation to  $\alpha'$  from  $\gamma$  taking place before the bulk transformation and is associated with the difference in carbon contents of  $\gamma$  at the end of IA.  $\gamma$  can nucleate from different phases in heterogenous microstructure, which can sometimes lead to slightly different carbon contents in small fraction of  $\gamma$  islands; similar phenomena were also noticed by Grajcar et al.<sup>[4,3]</sup>

## 4. Discussion

For maintaining clarity, the discussion is divided into two sections: effect of changing the cooling cycle and effect of changing the PT. Abbreviations for phases are not used in the following section to enhance the readability.

### 4.1. Effect of Cooling Cycle

The results obtained after IAQ&P treatments suggest that the starting microstructure influences the final phase fractions and microstructure. Route A and B samples exhibited increased strength and uniform elongation, whereas route C samples noted a reduction in strength (Figure 8). The enhanced strength observed in route A and B samples was attributed to the high fraction of martensite and the optimal fraction of retained austenite. In order to obtain optimum fraction of retained austenite in a Q&P treatment, formation of sufficient amount of martensite is necessary at the interrupted quenching stage allowing partition of carbon to austenite during the partitioning stage.<sup>[3,4]</sup> XRD results (Figure 7) reveal that route C samples exhibit low amount of retained austenite at room temperature in comparison with route A and B counterparts. From the SEM and EBSD micrographs (Figure 9 and 10, respectively), it can be confirmed that route C samples mainly consist of ferrite while route A and B samples contain large fraction of martensite (either primary or secondary), some ferrite and retained austenite. The main reason for the low fraction of retained austenite in route C samples is the

small amount of martensite formed at the interrupted QT, resulting in insufficient stability of retained austenite at the end of partitioning stage. Low amount of martensite in route C samples led to low yield strength (Figure 8) while large fraction of soft polygonal ferrite contributed to high elongation.

Results obtained from dilatometry experiments show that starting microstructure can suppress or increase the  $A_{c1}$  transformation temperature leading to varying fraction of austenite at the end of IA and thus leading to different amount of martensite at QT. This phenomenon is especially evident from route C samples, which had little martensite because of the low amount of austenite at the completion of IA. The reason is that nucleation of austenite occurs at a lower temperature from a microstructure consisting of majorly bainite and small amount of martensite (route A) and from a mixture of ferrite, martensite, austenite, and cementite (route B) while nucleation of austenite occurs at a higher temperature from a microstructure consisting of mainly ferrite (route C). Esin et al.<sup>[25]</sup> also reported that austenite formation from a ferrite–pearlite microstructure occurs at a higher temperature as compared to a tempered martensite or bainite microstructure. They explained that martensite and/or bainite consist of high density of interfaces; moreover, laths of martensite and sheaves of bainite represent shorter diffusion distances compared to pearlite. The nucleation of austenite from a martensitic microstructure was studied by Wei et al.<sup>[24]</sup> who observed that fraction of austenite exceeded the equilibrium fraction during intercritical annealing from a quenched martensite microstructure. It is clear that austenite fraction is high at the end of IA in route A and B samples compared to route C samples.

Combined analysis from the results of XRD (Figure 7), tensile tests (Figure 8), SEM (Figure 9), and EBSD (Figure 10) shows that mechanical properties depend on amount of martensite formed at the interrupted quenching stage in a IAQ&P treatment. Comparison of the micrographs and mechanical properties of the samples from A, B, and C routes showed that varying phase fraction imparted different mechanical properties. Similar results were also reported by Seo et al.<sup>[15]</sup> and Kantanen et al.<sup>[44]</sup> It was observed that martensite formed at the quenching stage depends on the prior austenite fraction (at the end of IA) and the prior austenite fraction can vary with the different initial cold-rolled microstructure; this is in line with the study by Chen et al.<sup>[45]</sup> Starting microstructure effects the nucleation and growth mechanism of austenite which can then lead to higher or lower fraction of austenite than equilibrium fraction at IAT. The effect of initial microstructure was particularly evident for route C samples which formed low austenite fraction at the end of IA leading to low amount of martensite and resulting in subsequently low strength. This means that when conducting and designing IAQ&P treatment, hot rolling and cooling methods must be taken into account as it effects the prior austenite fraction because the phases are influenced not only by the choice of QT but also by the starting microstructure.

#### 4.2. Effect of Partitioning Temperature

With the utilized characterization methods, it appears as though samples partitioned at 450 °C contain more secondary

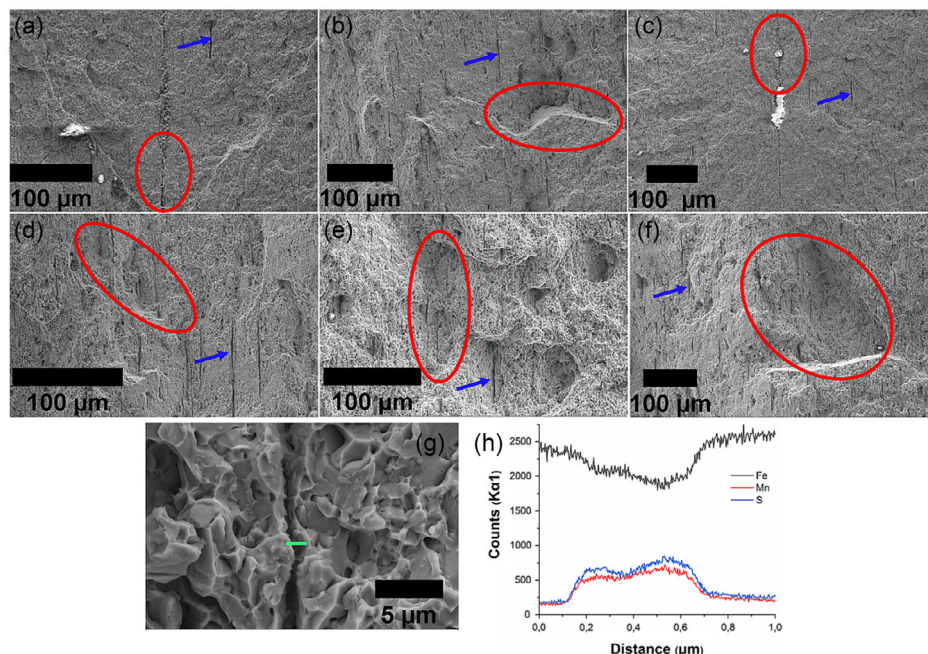


**Figure 12.** Fracture surface of the samples a) 1B\_60 $\gamma$ \_450, b) 1B\_60 $\gamma$ \_400, c) 2A\_60 $\gamma$ \_450, d) 2A\_60 $\gamma$ \_400, e) 2C\_70 $\gamma$ \_450, f) 2C\_70 $\gamma$ \_400, and g) magnified image of 1B\_60 $\gamma$ \_450; green line at the crack shows from where the EDS line analysis was conducted; h) result from EDS line analysis from the area shown in (g).

martensite; however, further investigations were conducted to investigate the presence of secondary martensite. The fracture surfaces of selected tensile test samples were examined by SEM; Figure 12a–f shows the micrographs. The red oval in the micrographs shows the origin of the fracture and gives information on fracture mode. The samples 1B\_60 $\gamma$ \_450 (Figure 12a) and 2A\_60 $\gamma$ \_450 (Figure 12c) exhibit brittle fracture. The brittle fracture confirms the presence of secondary martensite in samples partitioned at 450 °C. The micrographs of samples 1B\_60 $\gamma$ \_400 and 2A\_60 $\gamma$ \_400 (Figure 12b,d, respectively) show a dimpled ductile fracture. The reason is lack of secondary martensite in samples partitioned at 400 °C. The route C samples, Figure 12e,f, shows large dimples on the fracture surfaces, shows ductile fracture. The reason of ductile fracture is high amount of ferrite in both route C samples partitioned at 400 and 450 °C. In Figure 12a–f, there are small cracks (shown by blue arrow) that are visible in all samples. EDS line analysis was conducted on these cracks. Figure 12g shows a magnified image of the crack shown in Figure 12a and the green horizontal line in Figure 12g shows where the line analysis was taken from. The line analysis confirms that these small cracks are formed due to manganese sulfide (MnS) in both steel samples (Figure 12h). There was no evidence that these cracks had significant effect on the fracture behavior and final mechanical properties.

Samples from routes A and B partitioned at 400 °C show good combination of strength and ductility while samples partitioned at 450 °C exhibited brittleness. Brittle characteristics were primarily due to the presence of secondary martensite. Partitioning at 450 °C somehow facilitates the formation of secondary martensite and suppresses the fraction of retained austenite. The study by Knijf et al.<sup>[46]</sup> shows that partitioning between 370 and 400 °C facilitated the diffusivity of carbon in austenite. The effect of adopting a higher PT in a Q&P process was also investigated by Ebner et al.<sup>[47]</sup> who noticed the precipitation of “ $\theta$  and  $\chi$ ” type carbides when the PT was above 400 °C. The change in PT had little effect on the route C samples because of insufficient fraction of martensite formed at quenching. This indicates that effect of PT is only visible when sufficient amount of martensite is formed, or in other words, carbon partition to retained austenite is facilitated when fraction of martensite is sufficient.

Collective findings from the characterization techniques entail that mechanical properties can be optimized in an IAQ&P-treated steel by modifying the cooling cycle after hot rolling. Strength and elongation characteristics are dependent on the phase fraction of martensite formed at QT and if there is an adequate fraction of martensite, then adopting a suitable partitioning temperature would lead to successful stabilization of retained austenite at room temperature resulting in good balance of strength and elongation.

## 5. Conclusions

The microstructural characteristics and mechanical properties of two different low-carbon medium-manganese aluminum-alloyed steels undergone three different thermomechanical treatments were investigated by conducting IAQ&P heat treatments. The main findings and conclusions can be summarized as follows: 1) It is possible to enhance strength and elongation of cold-rolled and annealed medium-manganese aluminum containing steels by altering the thermomechanical parameters subsequent to hot rolling. Highest tensile strength of 1500 MPa with uniform elongation of 12% was achieved attributed to alterations in the cooling cycle. 2) The fraction of austenite at the end of intercritical annealing is not only a function of the nominal composition but also depends on the starting microstructure. The  $A_{c1}$  phase transformation temperature was influenced by the starting microstructure and chemical composition, leading to variations in the fraction of austenite formed at the respective IAT for 240 s. 3) The stabilization of retained austenite at room temperature depends on the selection of PT. The PT of 400 °C was suitable to obtain sufficient fraction of retained austenite at room temperature while partitioning at 450 °C resulted in the suppression of retained austenite and increment of secondary martensite. Furthermore, the effect of changing the PT was minimal in samples with an initial ferritic microstructure because sufficient amount of martensite did not form at the interrupted QT.

## Appendices

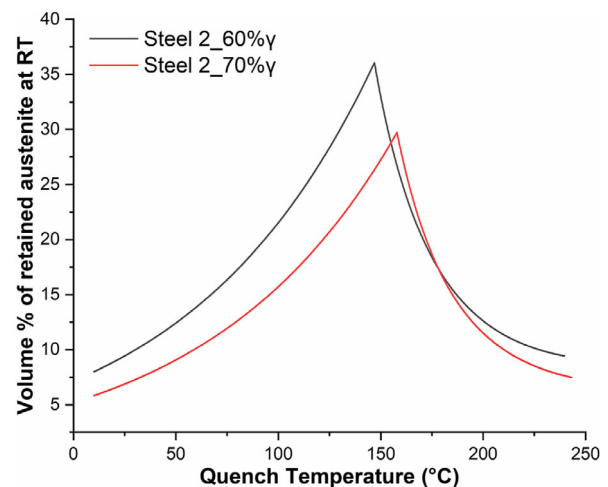


**Figure A1.** Calculation of volume percentage of retained austenite for steel 2 as a function of quenching temperature at the prior austenite fraction of 60% and 70%. Due to overlapping, the curves for steel 1 are not included in the figure.

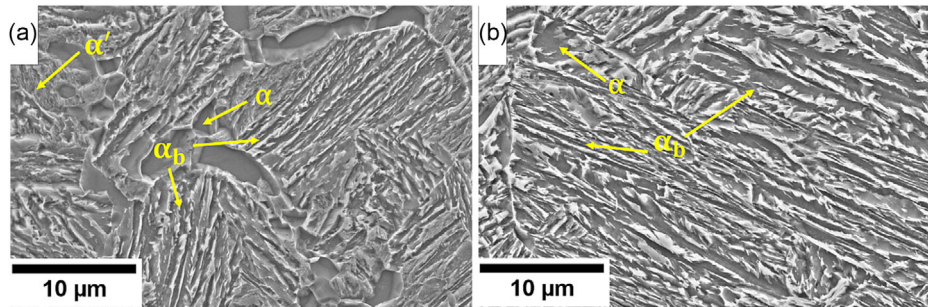


**Figure A2.** High-resolution micrographs of a) steel 1 and b) steel 2 from route A.

## Acknowledgements

The authors would like to acknowledge the efforts of Juha Uusitalo for conducting Gleeble experiments. The authors are grateful to Petri Jussila and Martti Järvenpää from SSAB for their suggestions. This work made use of Tampere Microscopy Center (TMC) facilities at Tampere University.

## Conflict of Interest

The authors declare no conflict of interest.

## Data Availability Statement

The data that support the findings of this study are available from the corresponding author upon reasonable request.

## Keywords

effect of starting microstructures, medium-manganese steels, phase fractions, quenching and partitioning heat treatments

Received: May 23, 2024  
Revised: September 6, 2024  
Published online:

- [1] S. Mohapatra, G. Poojari, S. Das, K. Das, *Mater. Sci. Eng. A* **2023**, 887 145769.
- [2] L. Liu, B. He, M. Huang, *Adv. Eng. Mater.* **2018**, 20, 1701083.
- [3] J. G. Speer, A. M. Streicher, D. Matlock, F. Rizzo, G. Krauss, in *Symp. on Thermodynamics, Kinetics, Characterization and Modelling of Austenite Formation and Decomposition*, ISS and TMS, Chicago, **2003**, p. 505.
- [4] J. G. Speer, F. C. Rizzo Assunção, D. K. Matlock, D. V. Edmonds, *Mater. Res.* **2005**, 8, 417.
- [5] S. Yan, X. Liu, W. J. Liu, T. Liang, B. Zhang, L. Liu, *Mater. Sci. Eng. A* **2017**, 684, 261.
- [6] D. H. Kim, J.-H. Kang, J. H. Ryu, S.-J. Kim, *Mater. Sci. Technol.* **2019**, 35, 2115.
- [7] E. J. Seo, L. Cho, Y. Estrin, B. C. De Cooman, *Acta Mater.* **2016**, 113, 124.
- [8] A. Arlazarov, M. Ollat, J. P. Masse, M. Bouzat, *Mater. Sci. Eng. A* **2016**, 661, 79.
- [9] S. Ayenampudi, C. Celada-Casero, J. Sietsma, M. J. Santofimia, *Materia* **2019**, 8, 100492.
- [10] Y. Y. Cheng, G. Zhao, D. M. Xu, X. P. Mao, S. Q. Bao, G. W. Yang, *J. Mater. Res. Technol.* **2022**, 20, 1226.
- [11] T. Nyyssönen, P. Peura, E. D. Moor, D. Williamson, V. T. Kuokkala, *Mater. Charact.* **2019**, 148, 71.
- [12] T. Nyyssönen, O. Oja, P. Jussila, A. Saastamoinen, M. Somani, P. Peura, *Metals* **2019**, 9, 9030373.
- [13] O. Oja, P. Jussila, S. Ahmed, M. Patnamsetty, P. Peura, in *International Conf. on Steels in Cars and Trucks*, Salz. Mann. Forsch., Italy, **2022**, p. 139.
- [14] J. Li, Y. Xu, B. Lu, Y. Yu, Y. Jing, W. Sun, *J. Mater. Res. Technol.* **2022**, 18, 352.
- [15] E. J. Seo, L. Cho, B. C. De Cooman, *Metall. Mater. Trans. A* **2015**, 46A, 27.
- [16] X. X. Dong, Y. F. Shen, N. Jia, W. Y. Xue, *Mater. Sci. Eng. A* **2023**, 869, 144791.
- [17] D. De Knijf, R. Petrov, C. Föjer, L. A. I. Kestens, *Mater. Sci. Eng. A* **2014**, 615, 107.
- [18] M. Gouné, S. Aoued, F. Danoix, G. Geandier, A. Poulon-Quintin, J. C. Hell, *Scr. Mater.* **2019**, 162, 181.
- [19] G. R. Speich, V. A. Demarest, R. L. Miller, *Metall. Trans. A* **1981**, 12, 1419.
- [20] J. Huang, W. J. Poole, M. Militzer, *Metall. Mater. Trans. A* **2004**, 35, 3363.
- [21] J. J. Mueller, X. Hu, X. Sun, Y. Ren, K. Choi, E. Barker, J. G. Speer, D. K. Matlock, E. De Moor, *Mater. Des.* **2021**, 203, 109598.
- [22] J. A. Mathews, J. Sietsma, R. H. Petrov, M. J. Santofimia, *J. Mater. Res. Technol.* **2023**, 25, 5325.
- [23] J. Teixeira, M. Moreno, S. Y. P. Allain, C. Oberbillig, G. Geandier, F. Bonnet, *Acta Mater.* **2021**, 212, 116920.
- [24] R. Wei, M. Enomoto, R. Hadian, H. S. Zurob, G. R. Purdy, *Acta Mater.* **2013**, 61, 697.
- [25] V. A. Esin, B. Denand, Q. L. Bihan, M. Dehmas, J. Teixeira, G. Geandier, S. Denis, T. Sourmail, E. Aebly-Gautier, *Acta Mater.* **2014**, 80, 118.
- [26] M. Krbata, D. Krizan, M. Eckert, S. Kaar, A. Dubec, R. Ciger, *Mater.* **2022**, 15, 1753.
- [27] S. Mohapatra, A. Mandal, S. Das, K. Das, *Mater. Sci. Eng. A* **2024**, 894, 146225.
- [28] S. Ahmed, J. Penttilä, J. Rämö, M. Honkanen, V. T. Kuokkala, O. Oja, P. Peura, *Mater. Sci. Eng.* **2022**, 856, 144011.
- [29] Y. Granbom, *Steel. Res. Int.* **2008**, 79, 297.
- [30] D. V. Edmonds, K. He, F. C. Rizzo, B. C. De Cooman, D. K. Matlock, J. G. Speer, *Mater. Sci. Eng. A* **2006**, 438–440, 25.
- [31] D. P. Koistinen, R. E. Marburger, *Acta Metall.* **1959**, 7, 59.
- [32] C. Capdevila, F. Caballero, C. García de Andrés, *ISIJ Int.* **2002**, 42, 894.
- [33] ASTM Committee, *Standard E0975-13*, **1984**, USA pp. 1–7.

- [34] D. J. Dyson, *J. Iron Steel Inst.* **1970**, *208*, 469.
- [35] G. Krauss, S. W. Thompson, *ISIJ Int.* **1995**, *35*, 937.
- [36] N. Fonstein, M. Kapustin, N. Pottore, I. Gupta, O. Yakubovsky, *Phys. Met. Metallogr.* **2007**, *104*, 315.
- [37] C. Y. Wang, J. Shi, W. Q. Cao, H. Dong, *Mater. Sci. Eng. A* **2010**, *527*, 3442.
- [38] X. C. Xiong, B. Chen, M. X. Huang, J. F. Wang, L. Wang, *Scr. Mater.* **2013**, *68*, 321.
- [39] H. K. D. H. Bhadeshia, D. V. Edmonds, *Met. Sci.* **1983**, *17*, 411.
- [40] M. Takahashi, H. K. D. H. Bhadeshia, *J.I.M.* **1991**, *32*, 689.
- [41] C. Song, H. Yu, L. Li, T. Zhou, J. Lu, X. Liu, *Mater. Sci. Eng. A* **2016**, *670*, 326.
- [42] G. E. Totten, in *Steel Heat Treatment, Metallurgy and Technologies*, 2nd ed., CRC Press, Boca Raton, FL **2006**.
- [43] A. Grajcar, M. Morawiec, J. A. Jimenez, C. Garcia-Mateo, *Mater.* **2020**, *13*, 4442.
- [44] P. Kantanen, M. Somani, A. Kaijalainen, O. Haiko, D. Porter, J. Kömi, *Metals* **2019**, *9*, 256.
- [45] B. Chen, J. Liang, T. Kang, R. Cao, C. Li, J. Liang, F. Li, Z. Zhao, D. Tang, *Metals* **2018**, *8*, 8080579.
- [46] D. De Knijf, E. P. Da Silva, C. Föjer, R. Petrov, *Mater. Sci. Technol.* **2015**, *31*, 817.
- [47] S. Ebner, R. Schnitzer, C. Suppan, A. Stark, H. Liu, C. Hofer, *Mater. Charact.* **2020**, *163*, 110242.